Experimental evidence consistent with a magnon Nernst effect in the antiferromagnetic insulator MnPS_{3}

Y. Shiomi, R. Takashima, and E. Saitoh

Phys. Rev. B **96**, 134425 — Published 25 October 2017

DOI: 10.1103/PhysRevB.96.134425

Experimental evidence consistent with magnon Nernst effect in an antiferromagnetic insulator $MnPS_3$

Y. Shiomi[1], R. Takashima[2], and E. Saitoh[1,3,4,5]

[1] *Institute for Materials Research, Tohoku University, Sendai 980-8577, Japan*

[2] *Department of Physics, Kyoto University, Kyoto 606-8502, Japan*

[3] *WPI Advanced Institute for Materials Research, Tohoku University, Sendai 980-8577, Japan*

[4] *Advanced Science Research Center, Japan Atomic Energy Agency, Tokai 319-1195, Japan and*

[5] *Center for Spintronics Research Network, Tohoku University, Sendai 980-8577, Japan*

(Dated: October 10, 2017)

Abstract

A magnon Nernst effect, an antiferromagnetic analogue of the magnon Hall effect in ferromagnetic insulators, has been studied experimentally for a layered antiferromagnetic insulator $MnPS_3$ in contact with two Pt strips. Thermoelectric voltage in the Pt strips grown on $MnPS_3$ single crystals exhibits non-monotonic temperature dependence at low temperatures, which is unlikely to be explained by electronic origins in Pt but can be ascribed to the inverse spin Hall voltage induced by a magnon Nernst effect. Control of antiferromagnetic domains in the $MnPS_3$ crystal by magnetoelectric cooling is found to modulate the low-temperature thermoelectric voltage in Pt, which is evidence consistent with the emergence of the magnon Nernst effect in Pt|$MnPS_3$ hybrid structures.

I. INTRODUCTION

Berry phase is a fundamental concept in solid state physics and responsible for a spectrum of physical phenomena [1]. One pronounced example caused by Berry phase is Hall effects of electrons. The Berry curvature of electrons is made manifest as transverse velocity of the electrons, which gives rise to various Hall effects, *e.g.* anomalous Hall effects, topological Hall effects, and spin Hall effects [1–3]. In semi-classical theory, the Berry curvature can be regarded as an effective magnetic flux for conduction electrons, and the related effective Lorentz force bends the trajectory of moving electrons to the Hall direction [1–3].

Recently, the Berry phase concept has been expanded to magnon transport in ferromagnetic insulators [4, 5]. In insulating magnets, the spin transport is governed by low-energy spin excitations, *i.e.* magnons. The ring exchange process on ferromagnetic lattices leads to a Berry phase effect in magnon transport [4]. With certain types of lattice geometry and magnetic order, the net fictitious magnetic field due to the magnon Berry curvature survives, and there occurs the magnon Hall effect [4, 5]. As shown in Fig. 1(a), the magnon Hall current produces temperature gradient along the Hall direction, leading to finite thermal Hall conductivity. The magnon Hall effect has been demonstrated experimentally by the measurement of the thermal Hall effect (Righi-Leduc effect) for a pyrochlore ferromagnet $Lu_2V_2O_7$ [6] and other magnetic insulators [7–9].

In this letter, the topological magnon transport induced by the Berry curvature is experimentally expanded to antiferromagnetic insulators: magnon-mediated spin Nernst effect, dubbed as magnon Nernst effect [10, 11]. In a honeycomb antiferromagnet in the presence of the Dzyaloshinskii-Moriya (DM) interaction, a longitudinal temperature gradient can give rise to spin currents along the Hall direction, realizing a magnon Nernst effect [10, 11]. This effect can be viewed as an antiferromagnetic analogue of the magnon Hall effect in ferromagnetic insulators, which stems from a fictitious magnetic flux due to the magnon Berry curvature. As shown in Fig. 1(b), in a honeycomb antiferromagnet [10, 11], both up-spin and down-spin magnons exhibit the magnon Hall effect under an applied inplane temperature gradient, but magnons with opposite spins flow in opposite transverse directions. The thermal Hall current thereby cancels out, while a nonzero spin current emerges in the Hall direction. Generation of spin currents devoid of a thermal current without external magnetic fields should be a significant merit of antiferromagnetic spintronics [12].

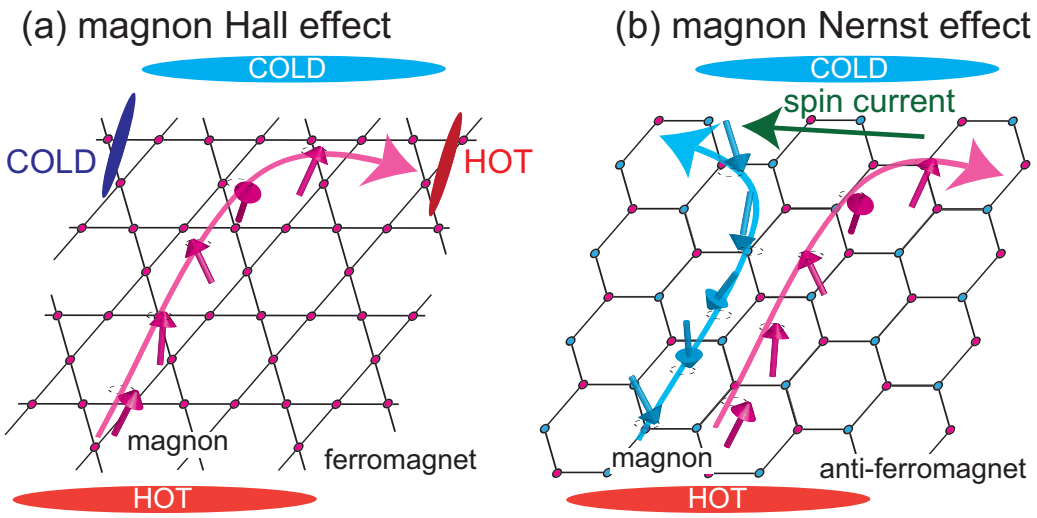

FIG. 1: Schematics of (a) the magnon Hall effect in kagome ferromagnets and (b) the magnon Nernst effect in honeycomb antiferromagnets.

As a material candidate to realize magnon Nernst effects, monolayer $MnPS_3$ has been theoretically discussed [10] and non-monotonic temperature dependence of the magnon Nernst coefficient was predicted based on a low-temperature spin-wave approximation [see Fig. 4(d)]. Though growth of the monolayer $MnPS_3$ is experimentally challenging, the similar effect is expected in bulk $MnPS_3$ because of the two-dimensional crystal structure with tiny interlayer magnetic couplings [13]. Bulk single crystals of $MnPS_3$ have been intensively studied because of the two-dimensional character in the magnetic properties [14] and the easy intercalation of lithium and molecules [15]. In order to study magnon Nernst effects expected in $MnPS_3$, we here prepare bulk single crystals of $MnPS_3$ and employ the technique of the inverse spin Hall effect [16] for electrical detection of the transverse spin current induced by the magnon Nernst effect. For Pt films grown on the edges of $MnPS_3$ single crystals, we have observed non-monotonic temperature dependence of the thermoelectric voltage and also its dependence on antiferromagnetic domains of $MnPS_3$. These results indicate that the magnon Nernst effect induces inverse spin Hall voltage in the Pt|$MnPS_3$ structure.

II. EXPERIMENTAL METHOD

Bulk single crystals of $MnPS_3$ were grown by a chemical vapor transport method following a previous report [17]. Stoichiometric amounts totaling 5 g of Mn, P, and S elements were

sealed into an evacuated quartz tube. The tube was placed in a horizontal three-zone furnace and heated slowly up to 630-680 °C; the temperature of the charge region was set at 680 °C and that of the growth region at 630 °C. A number of plate-like single crystals of $MnPS_3$ were obtained in the growth region in 100 hours. As shown in Fig. 2(a), the $MnPS_3$ single crystals are optically transparent with a green color. The largest surfaces of the crystals were determined by x-ray diffraction measurements to be the *ab* plane, as shown in Fig. 2(b). Manganese ions (Mn^{2+}) form a honeycomb lattice within the *ab* plane and the honeycomb lattices are stacked along the *c* direction with a weak Van-der-Waals interlayer coupling [15].

The $MnPS_3$ single crystals are highly insulating below room temperature, which is suitable for studying spin-current generation free from magneto-transport effects inside $MnPS_3$. The magnetic property of $MnPS_3$ was studied using a SQUID magnetometer (Magnetic Property Measurement System; Quantum Design, Inc.). The temperature (T) dependence of the magnetization, M, for a $MnPS_3$ single crystal is shown in Fig. 2(c). Here, the external magnetic field (H) of 1 T was applied perpendicular to the crystal plane. With decreasing T from 300 K, M increases and shows a broad peak around 110 K, reflecting a short range order of Mn^{2+} spins [17]. The magnetization sharply decreases below 80 K, which corresponds to the antiferromagnetic ordering temperature of Mn^{2+} spins (T_N). Each Mn^{2+} spin in the *ab* plane is coupled antiferromagnetically with the nearest neighbors and coupled ferromagnetically with the interlayer neighbors [17]. The observed M-T curve [Fig. 2(c)] is similar to that reported previously [17], which supports the high quality of our single crystals.

Seemingly homogeneous crystals of $MnPS_3$ were selected and used for the measurement of the magnon Nernst effect. Since $MnPS_3$ single crystals are soft and fragile, the surface treatment by mechanical polish is difficult, and then Ar-ion milling was applied. As illustrated in Fig. 2(d), $MnPS_3$ crystals were irradiated with Ar ions at an acceleration voltage of 500 V at 45° angles to the crystal planes for 30 minutes on a water cooled sample holder. The irradiation was done in the intervals of 10 minutes with a pause of time longer than 10 minutes in order to avoid sample damages. On both the edges of $MnPS_3$ surfaces, 5-nm-thick Pt films (with the size of $\sim 4 \times 1$ mm^2) were sputtered at room temperature in an Ar atmosphere, as shown in Fig. 2(d). Since the edges of $MnPS_3$ surfaces were made inclined naturally and/or by Ar ion milling, the spin current flowing along a Hall direction in $MnPS_3$ can be detected using the inverse spin Hall effect in Pt.

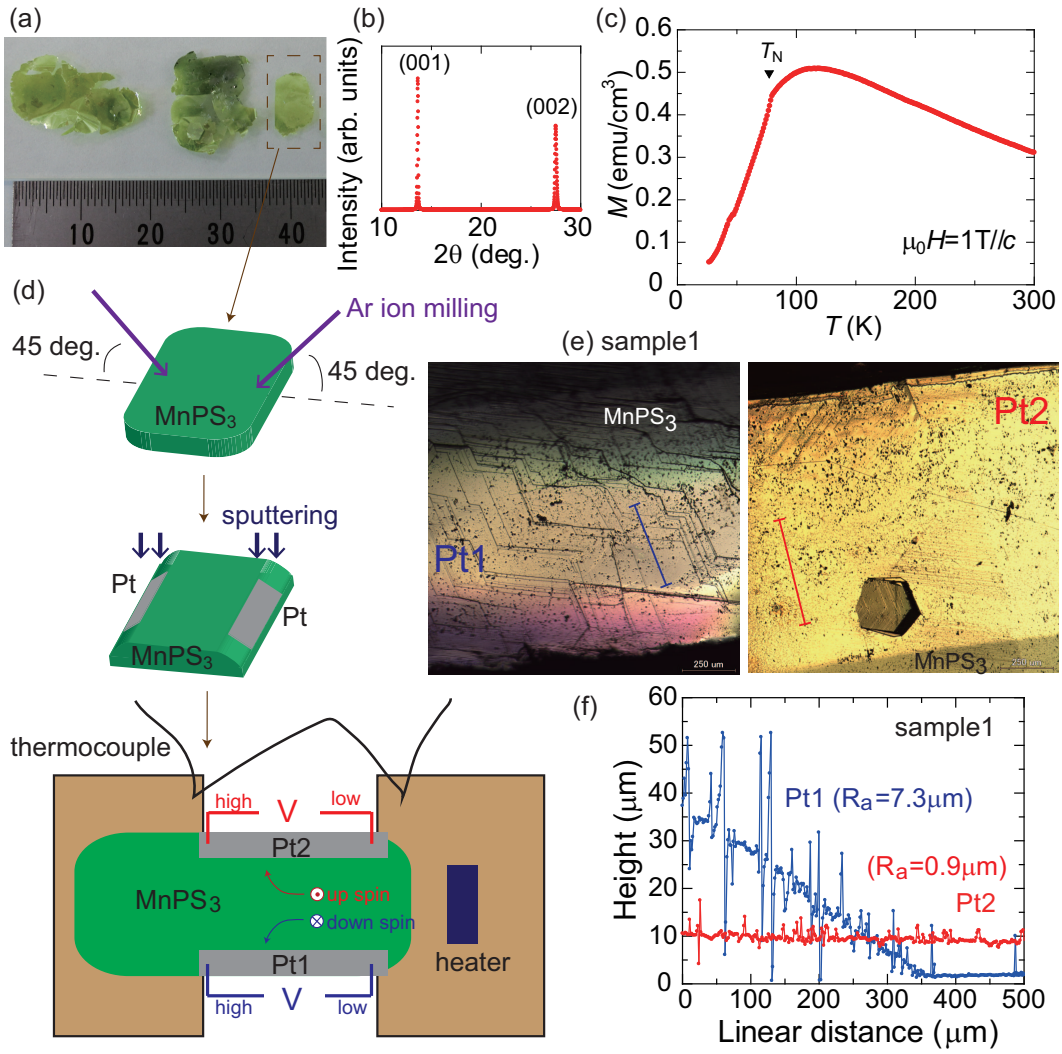

FIG. 2: (a) Examples of $MnPS_3$ single crystals. (b) X-ray diffraction pattern of a $MnPS_3$ single crystal. (c) Temperature (T) dependence of the magnetization (M) for a $MnPS_3$ single crystal. The measurement was performed under magnetic fields of 1 T applied along the c axis. (d) Flow chart of sample setup in the magnon Nernst effect measurement. After the surface treatment by Ar-ion milling processes, 5-nm-thick Pt films were deposited on the $MnPS_3$ surfaces. The Pt|$MnPS_3$ samples were fixed on two heat sinks for the measurement of thermoelectric voltages. (e) Surface images taken with a laser microscope for Pt1 and Pt2 of Sample1. (f) Distance distribution of surface heights for Pt1 and Pt2 of Sample1. This graph is obtained from the images shown in (e).

The obtained Pt|$MnPS_3$ structures were fixed on two heat sinks using GE varnish, as shown in Fig. 2(d); on one heat sink, a 1kΩ chip resistor was put to generate temperature gradient in an inplane direction. The temperature difference between the two heat sinks, ΔT, was measured with a couple of type-E thermocouples. The thermoelectric voltage, V, measured with ϕ-25μm Au wires for the two Pt strips (denoted by Pt1 and Pt2 hereafter)

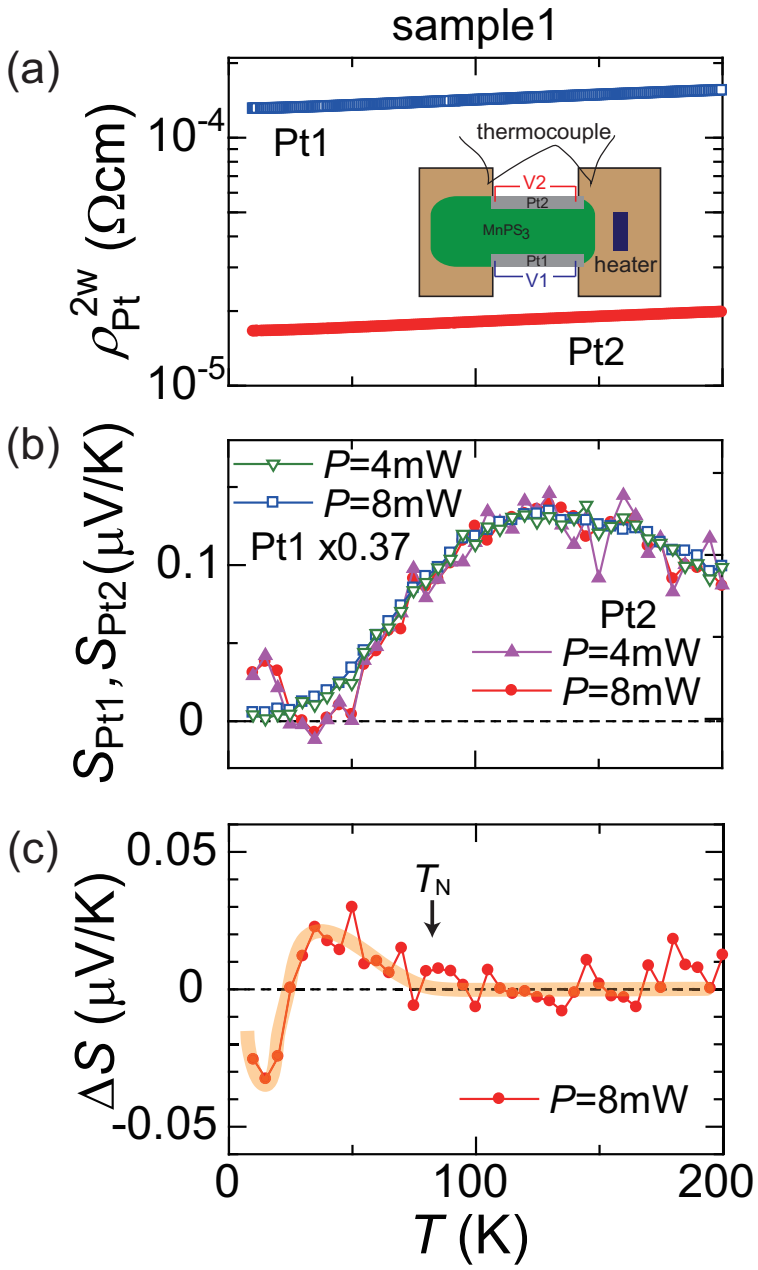

FIG. 3: Temperature (T) dependence of (a) two-wire resistivity ($\rho_{\rm Pt}^{\rm 2w}$) for Pt1 and Pt2 of Sample1, (b) $V/\Delta T$ for Pt1 and Pt2 of Sample1 ($S_{\rm Pt1}$ and $S_{\rm Pt2}$, respectively), and (c) the anomalous thermoelectric contribution defined as $\Delta S \equiv 0.37 \times S_{\rm Pt1} - S_{\rm Pt2}$ for Sample1. In (b), $0.37 \times S_{\rm Pt1}$ at each T is plotted for Pt1. Here, P in (b) and (c) denotes the power level applied to the heater.

was recorded with Keithly 2182A nanovoltmeters. The measurements were performed in a cryogenic probe station in the temperature range between 10 K and 200 K without external magnetic fields. Note that the values of ΔT in the thermoelectric measurements are shown in Appendix sections.

III. RESULTS

Figure 3 shows a set of experimental results for Sample1 of Pt|$MnPS_3$. In Fig. 3(a), two-wire resistivity, $\rho_{\rm Pt}^{\rm 2w}$, measured between the voltage electrodes for Pt1 and Pt2 was presented. For Pt2, $\rho_{\rm Pt}^{\rm 2w}$ is lower than 2×10^{-5} Ωcm, which is almost the same as that of Pt films grown on an oxidized-Si substrate in our sputtering condition [18]. By contrast, $\rho_{\rm Pt}^{\rm 2w}$ for Pt1 is over 1×10^{-4} Ωcm, about ten times greater than that for Pt2. The difference in $\rho_{\rm Pt}^{\rm 2w}$ between Pt1 and Pt2 should be related with the roughness of the $MnPS_3$ surface, as shown in Figs. 2(e) and 2(f). Arithmetic average roughness (R_a) is 0.9 μm for Pt2|$MnPS_3$, while as large as 7.3 μm for Pt1|$MnPS_3$ in Fig. 2(e). The Pt2|$MnPS_3$ interface is much smoother than Pt1|$MnPS_3$; higher spin mixing conductance is expected at the Pt2|$MnPS_3$ interface.

Figure 3(b) shows T dependence of the thermoelectric coefficient for Pt1 and Pt2 strips of Sample1, $S_{\rm Pt1}$ and $S_{\rm Pt2}$. Here, $S_{\rm Pt1}$ and $S_{\rm Pt2}$ are defined by the thermoelectric voltage V divided by the temperature difference ΔT for Pt1 and Pt2 strips, respectively. Not only the Seebeck voltage of the Pt films but also the inverse spin Hall voltage induced by the magnon Nernst effect can contribute to $S_{\rm Pt1}$ and $S_{\rm Pt2}$ if it exists; note that the same sign of the magnon Nernst voltage is expected for Pt1 and Pt2 because the direction of spin polarization and also the direction of its flow are opposite between Pt1 and Pt2 [see Fig. 2(d)]. As shown in Fig. 3(b), $S_{\rm Pt1}$ and $S_{\rm Pt2}$ show a similar T dependence at high temperatures above T_N, while the magnitude of $S_{\rm Pt1}$ is larger than that of $S_{\rm Pt2}$ (see also Fig. 5). $S_{\rm Pt1}$ and $S_{\rm Pt2}$ exhibit the positive sign and show a broad peak around 120 K, which is consistent with the T dependence of the Seebeck coefficient for Pt bulk samples [19]. Hence, at high temperatures above T_N, the conventional Seebeck effect well explains $S_{\rm Pt1}$ and $S_{\rm Pt2}$.

At low temperatures below T_N, however, $S_{\rm Pt1}$ and $S_{\rm Pt2}$ totally show different T dependences. For high-resistive Pt1, $S_{\rm Pt1}$ monotonically decreases to zero as T decreases, as expected by the Seebeck effect in Pt [19]. In contrast, $S_{\rm Pt2}$ for low-resistive Pt2 shows a sign change from positive to negative at about 30 K, and then the sign changes again from negative to positive to exhibit a positive peak at 15 K. This highly non-monotinic T dependence of $S_{\rm Pt2}$ is unlikely to be explained by electronic origins of Pt, such as a change in dominant carriers at low temperatures, the phonon drag, or a magnetic secondary phase; such a complex electronic structure which can explain the serial sign changes (*i.e.* positive-negative-positive sign changes) is not observed in Pt, to the best of our knowledge. Also,

the Seebeck anomaly due to the phonon drag is observed as a single peak [20]. Furthermore, impurity transport does not explain the serial sign changes. Though a complicated T dependence of the Seebeck coefficient at low temperatures was reported *e.g.* in Pd with dilute magnetic Ni impurities (< 1 at%) [21], Mn impurities as much as ~ 1 at% in Pt films seem unlikely in our samples and resistivity anomaly as observed in the Pd-Ni alloys [22] is not recognized in the $\rho_{\rm Pt}^{\rm 2w}$-T curve in Fig. 3(a). In addition, since the measurement was done in zero magnetic field, the magnetic secondary phase does not exhibit anomalous Nernst or spin Seebeck effect. We also note that the sign changes of thermopowers in Pt may occur owing to local variations in Seebeck coefficients due to grain boundaries and other structural features, as discussed in metal nanowires [23, 24]. However, such grains and structural defects in Pt|$MnPS_3$ are insensitive to T, and thus difficult to explain the unconventional T dependence of $S_{\rm pt2}$ observed only in the limited T-range below T_N [Fig. 3(b)]. Hence, the anomalous T dependence observed in $S_{\rm pt2}$ below T_N is not explained by the simple modulation of the Seebeck voltages of Pt, impurity transport, or structural defects.

Notable is that the anomalous T dependence of $S_{\rm Pt2}$ at low temperatures below T_N is consistent with the theoretical prediction on the magnon Nernst effect for monolayer $MnPS_3$ [10]. In Fig. 3(c), the anomalous thermoelectric contribution in $S_{\rm Pt2}$ is separated from the conventional Seebeck effect by plotting $\Delta S \equiv 0.37 \times S_{\rm Pt1} - S_{\rm Pt2}$. As T decreases below T_N, ΔS evolves and shows a broad positive peak around 30 K, and then sharply drops to exhibit a sign change with a negative peak at 15 K. This T dependence of ΔS is consistent with that calculated theoretically for $MnPS_3$ in Fig. 4(d), where the sign change of the magnon Nernst voltage is predicted at 20 K-40 K by the sign flip of the magnon Berry curvature across the von Hove singularities [10]. The sign-change temperature of about 25 K corresponds to the DM parameter (D) of ≈ 0.3 meV (Appendix C).

As for the indiscernible magnon Nernst voltage in the Pt1 strip of Sample1 [Fig. 3(b) and Fig. 5], several possibilities can be raised. First, sizable roughness of $MnPS_3$ crystals as seen in Figs. 2(e) and 2(f) should decrease the spin mixing conductance between Pt and $MnPS_3$ layers, resulting in the suppression of the magnon Nernst voltage. In our experiments, the magnitude of $\rho_{\rm Pt}^{\rm 2w}$ strongly depends on samples. It is notable that $\rho_{\rm Pt}^{\rm 2w}$ for Pt2 of Sample1 is the lowest among our Pt|$MnPS_3$ samples, which indicates high spin mixing conductance. Second, the magnon Nernst voltage is expected to be smaller than the Seebeck voltage of Pt. Large Seebeck coefficients as observed in Pt1 of Sample1 are not suitable for the detection of

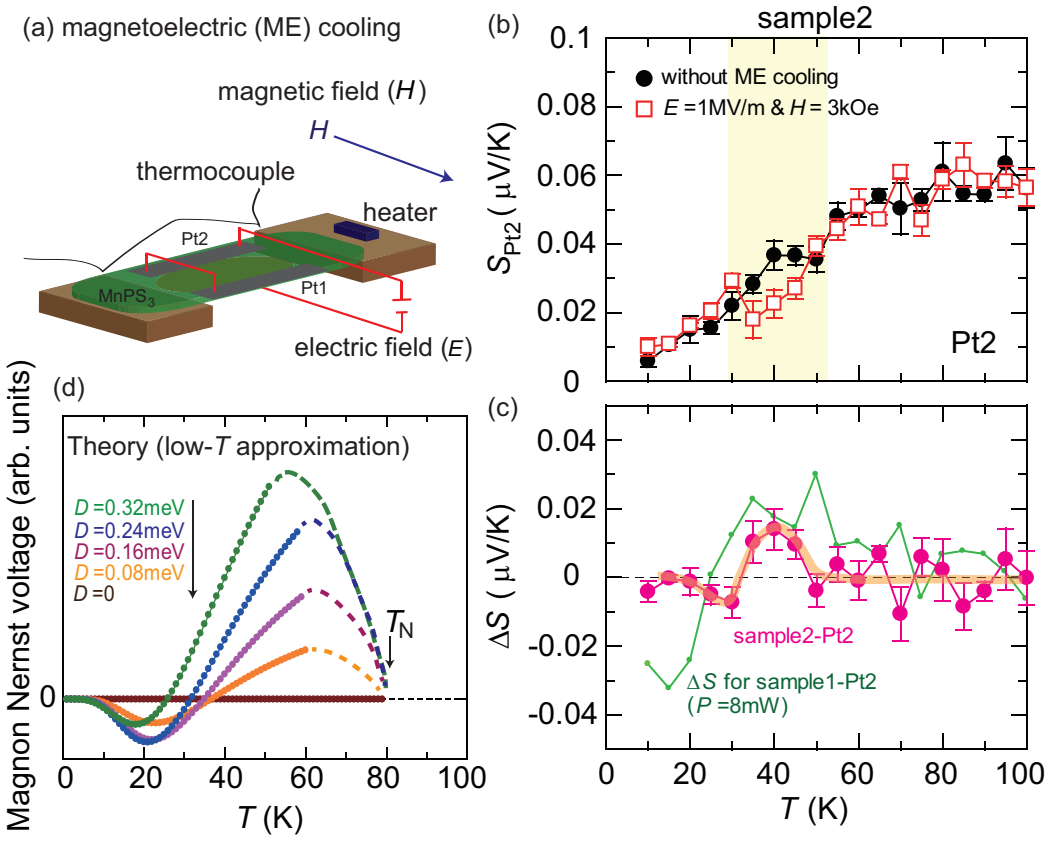

FIG. 4: (a) A schematic illustration of experimental configuration of magnetoelectric (ME) cooling. The electric field (E) is applied along the perpendicular-to-plane direction and the magnetic field (H) applied along an in-plane direction. (b) Temperature (T) dependence of $V/\Delta T$ for Pt2 ($S_{\rm Pt2}$) of Sample2 without ME cooling (circles) and after a ME cooling of $E = 1$ MV/m and $H = 3$ kOe (squares). (c) Temperature (T) dependence of the change of $S_{\rm Pt2}$ values by the ME cooling (ΔS) for Pt2 of Sample2 (circles). The data of ΔS for Pt2 of Sample1 at $P = 8$ mW is also shown for comparison. (d) Temperature (T) dependence of the magnon Nernst signal predicted theoretically for monolayer $MnPS_3$ [10]. The calculation is only valid at low temperatures, and the magnon Nernst signal should vanish above T_N of $MnPS_3$ as indicated by dotted curves.

small magnon Nernst voltage at low temperatures. Third, mixed antiferromagnetic domains whose boundaries disturb magnon transports can make the detection of the magnon Nernst voltage difficult.

To reveal the effect of antiferromagnetic domains in $MnPS_3$ on the magnon Nernst effect, we have investigated the dependence of the thermoelectric voltage on magnetoelectric (ME) cooling for Sample2 in Figs. 4(a)-4(c); here, $\rho_{\rm Pt}^{\rm 2w}$ and the Seebeck coefficient for Pt strips of Sample2 were relatively small among our samples (Figs. 4 and 6), but the magnon Nernst voltage was not observed within our experimental accuracy. It is known that $MnPS_3$ exhibits

a linear ME effect and that antiferromagnetic domains can be manipulated by cooling the sample under crossed magnetic and electric fields [25]. Although different antiferromagnetic domains are expected to produce the magnon Nernst voltage of the same sign (Appendix D), the multidomain states should reduce the magnon Nernst voltage because of disturbance of magnon transport by domain boundaries. Hence, the modulation of the thermoelectric voltage by ME cooling can corroborate the emergence of the magnon Nernst effect. As shown in Fig. 4(a), the $MnPS_3$ single crystal was submitted to electric and magnetic fields; the electric field (E) was applied along the perpendicular direction to the ab plane, while the magnetic field (H) along an inplane direction perpendicular to the Pt strips. Here, the gate-voltage electrode on the bottom surface was formed using a conductive silver paste [26] and the resistance between Pt strips and the bottom electrode was over the measurable range of multimeters. After ME cooling from 200 K down to 10 K under the simultaneous action of $E = 1$ MV/m (corresponding to 40 V) and $H = 3$ kOe, measurement of the thermoelectric voltages for Pt strips of Sample2 was performed without any fields in increasing-T scans, as shown in Fig. 4(b). To improve the signal-to-noise ratio, the measurements were repeated three times, and the averaged data sets with error bars (meaning the standard deviation) are shown in Fig. 4(b). Obviously, the value of S_{Pt2} after the ME cooling is found to be less than that measured without the ME cooling in the T range between 30 and 50 K, while it is less sensitive to the ME cooling in other T ranges. The change in the thermoelectric voltage of Pt by the ME cooling indicates that the voltage related with the antiferromagnetic domains in $MnPS_3$ is included in the thermoelectric voltage of Pt.

The change of the S_{Pt2} values by the ME cooling is calculated for Pt2 of Sample2, and is plotted against the measurement temperature, as shown in Fig. 4(c). A dome-shaped positive thermoelectric signal is tangible between 30 K and 50 K. Notably, the magnitude and T-dependence of the ΔS peak for Sample2 are similar to those of ΔS observed in Sample1 [Figs. 3(c) and 4(c)]. Note that, in the measurement for Sample2, the magnitudes of ΔT were set to be ~ 10 K at 10 K (Fig. 6) to improve the signal to noise ratio. Hence, the low-T negative peak as observed at 15 K for Pt2 of Sample1 in Fig. 3(c) is smeared for Pt2 of Sample2 owing to heating effects. The modulation of the thermoelectric voltage by ME cooling is evidence consistent with the emergence of the magnon Nernst effect for Pt|$MnPS_3$. The magnitude of the inverse spin Hall voltage induced by the magnon Nernst effect is at most several tens nanovolts in the present experiments.

IV. CONCLUSION

In summary, we measured thermoelectric voltages of Pt strips grown on the edges of $MnPS_3$ single crystals. The anomalous temperature dependence of the thermoelectric voltage for a low-resistive Pt strip on $MnPS_3$ is notably consistent with that of the magnon Nernst coefficient predicted in a theoretical work [10]. Furthermore, the modulation of the low-temperature thermoelectric voltage by magnetoelectric cooling was demonstrated, which shows that the thermoelectric voltage includes spin-related voltage signals dependent on antiferromagnetic domains of $MnPS_3$. The results signal the emergence of the magnon Nernst effect in the Pt|$MnPS_3$ samples. We hope that the present work will stimulate follow-up studies on the magnon Nernst effect in antiferromagnetic insulators to harmonize the spin caloritronics, antiferromagnetic spintronics, and topological spintronics.

ACKNOWLEDGEMENT

We are grateful to S. Daimon for informing Y. S. of a theoretical paper on the magnon spin Nernst effect [10]. This work was supported by JST ERATOgSpin Quantum Rectification Projecth (JPMJER1402), JSPS KAKENHI (No. 17H04806, No. JP16H00977, No. 16K13827, and No. 15J01700), and MEXT (Innovative Area "Nano Spin Conversion Science" (No. 26103005)).

Appendix A: Additional experimental data for Sample1

In Fig. 5, we show additional experimental results of the thermoelectric measurement for Sample1. Figure 5(a) shows temperature (T) dependence of the applied temperature difference, ΔT, in the thermoelectric measurement for Sample1. In the thermoelectric measurement, the heater power (P) was set to be constant at each T, and thereby the value of ΔT changes with T. The T dependence of S_{Pt1} and S_{Pt2} at $P = 4$ mW and 8 mW is shown in Fig. 3(b). At $P = 4$ mW, the ΔT magnitude is at most 2 K in the entire T range, and at $P = 8$ mW, at most 5 K, as shown in Fig. 5(a).

The T dependence of S_{Pt1} and S_{Pt2} at various heater-power (P) levels is shown in Figs. 5(b) and 5(c), respectively. As shown in Fig. 5(b), T dependence of S_{Pt1} is almost the same among all the P values from 4 mW to 32 mW. By contrast, S_{Pt2} at different P values clearly

shows different T dependences at the low-T range below $\sim$ 50 K. As clearly seen in Fig. 3(b), the two sign changes are observed in the T dependence of $S_{\rm Pt2}$ at $\sim$ 50 K and at $\sim$ 25 K for relatively-low P values. For very high P levels such as $P = 32$ mW, ΔT values reach $\sim$ 20 K at 10 K [Fig. 5(a)], and the sign changes are no longer observed in $S_{\rm Pt2}$ because of very strong heating effects of the sample; however, non-monotonic T dependence of $S_{\rm Pt2}$ is still observed below 50 K. Therefore, the anomaly due to the magnon Nernst effect is observed in T dependence of $S_{\rm Pt2}$ at all P values. It is notable that the similar signal of the magnon Nernst effect is observed in both increasing-T and decreasing-T scans. This is consistent with the theoretical prediction that the sign of the magnon Nernst effect is the same for different antiferromagnetic domains in $MnPS_3$ (see Appendix D).

Appendix B: Additional experimental data for Sample2

In Fig. 6, we show additional experimental results of the thermoelectric measurement for Sample2. As shown in Fig. 6(a), the magnitudes of two-wire resistivities ($\rho_{\rm Pt}^{\rm 2w}$) for Pt1 and Pt2 of Sample2 are similar, and almost two times higher than $\rho_{\rm Pt}^{\rm 2w}$ for Pt2 of Sample1 [Fig. 3(a)].

Figure 6(b) shows T dependence of the magnitude of ΔT in the thermoelectric measurement for Sample2. At $P = 2.25$ mW, the maximum value of ΔT is $\sim$ 5 K, while $\sim$ 10 K at $P = 4.5$ mW. The ΔT magnitudes applied for Sample2 are almost similar to those in the measurements done at $P = 8$ mW and 16 mW for Sample1, as shown in Fig. 5(a).

In Fig. 6(c), we show T dependence of $S_{\rm Pt1}$ for Sample2. The thermoelectric measurements were performed after two different T-cooled conditions: no ME cooling [circles in Fig. 6(c)] and ME cooling [squares in Fig. 6(c)]. As shown in Fig. 6(c), very small decrease in $S_{\rm Pt1}$ by ME cooling is observed for Pt1 in the T region between 30 K and 50 K, similar to the change observed for Pt2 of Sample2 in Fig. 4(b).

The change in $S_{\rm Pt1}$ by the ME cooling (ΔS) for Sample2 is plotted in Fig. 6(d). The error level is higher for Pt1 than Pt2, but a small positive ΔS signal is recognized for Pt1 in the T region between 30 K and 50 K. In fact, the background voltage in the thermoelectric measurement was as large as 1-1.5 μV for Pt1, while below 0.5 μV for Pt2; more precise measurements were thereby possible for Pt2 than Pt1. Also, several possibilities on the tiny magnitudes of magnon Nernst voltages in some Pt|$MnPS_3$ samples, *e.g.* Pt1 of Sample1,

are discussed in the Results section.

Appendix C: Estimation of the Dzyaloshinskii-Moriya (DM) parameter

The temperatures at which the sign of the magnon Nernst coefficient for monolayer $MnPS_3$ changes are calculated as a function of the magnitude of the Dzyaloshinskii-Moriya (DM) parameter (D), as shown in Fig. 7. Here, the antiferromagnetic exchange couplings up to the third nearest neighbors (J_1, J_2, J_3), the second nearest-neighbor DM interaction (D), and the easy-axis anisotropy are taken into account in this calculation, as reported in

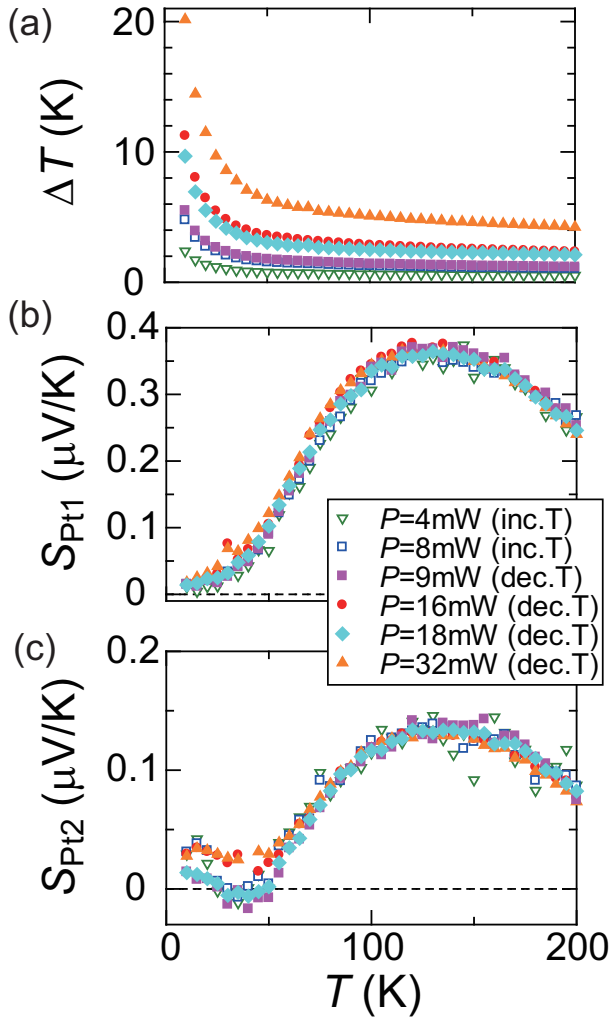

FIG. 5: Temperature (T) dependence of (a) the applied temperature difference (ΔT), (b) S_{Pt1} of Sample1, and (c) S_{Pt2} of Sample1. The experimental data at different heater-power (P) levels are distinguished by means of different symbols and colors.

[10]. As D increases, the sign-change temperature decreases [see also Fig. 4(d)]. In our experiments, the sign change of the magnon Nernst voltage is observed at 25-30 K in Figs. 3(c) and 4(c). This temperature corresponds to $D \approx 0.3$ meV.

Appendix D: On the sign of the magnon Nernst coefficient for two antiferromagnetic domains

The magnon Nernst coefficient is expected to be the same for two different antiferromagnetic domains which can coexist in $MnPS_3$ samples (Fig. 8). The magnon Nernst coefficient α^s_{xy} is defined by $\hbar(\boldsymbol{j}_\uparrow - \boldsymbol{j}_\downarrow)_y = (\partial_x T)\alpha^s_{xy}$, where $\boldsymbol{j}_{\uparrow/\downarrow}$ is the magnon current that carries ± 1 spin angular momentum along the $\hat{z}$ direction. The z direction is defined as the perpendicular direction to the ab plane of $MnPS_3$.

The magnon Nernst coefficient α^s_{xy} is considered to be invariant under space inversion,

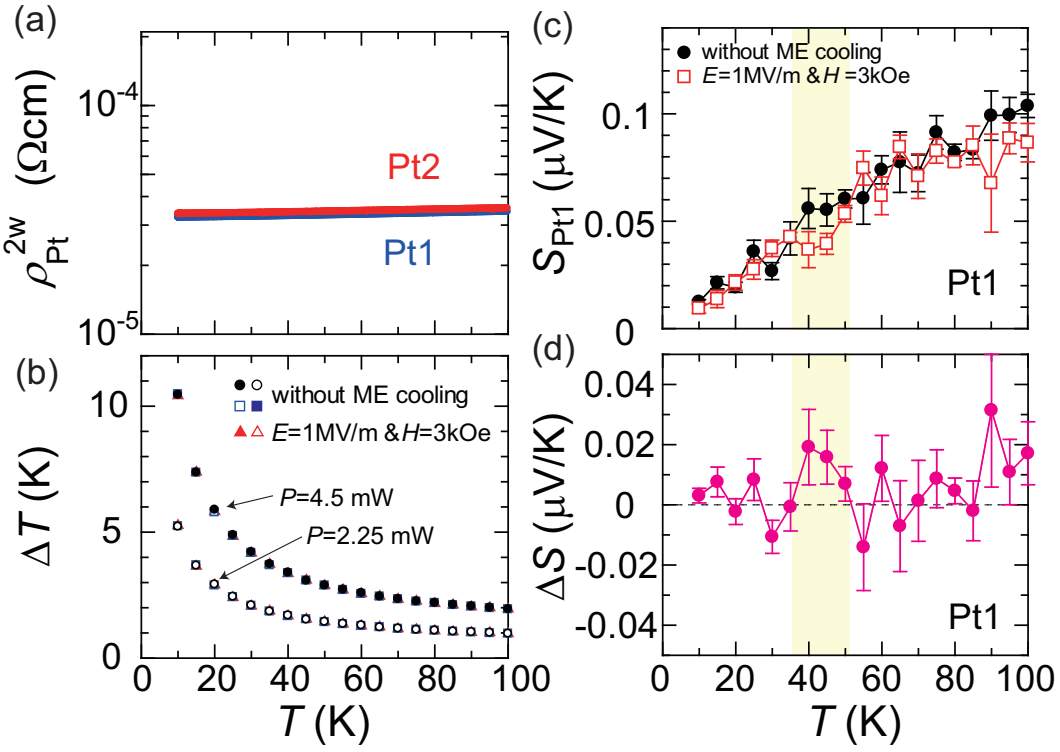

FIG. 6: Temperature (T) dependence of (a) two-wire resistivity (ρ^{2w}_{Pt}) for Pt1 and Pt2 of Sample2, (b) the applied temperature difference (ΔT) in the measurement of the magnon Nernst effect for Sample2, (c) S_{Pt1} of Sample2, and (d) the change in S_{Pt1} by the ME cooling (ΔS) for Sample2. In (c) and (d), the T range where the finite ΔS signal is observed in Pt1 and Pt2 of Sample2 [Fig. 4(c)] is highlighted by yellow color.

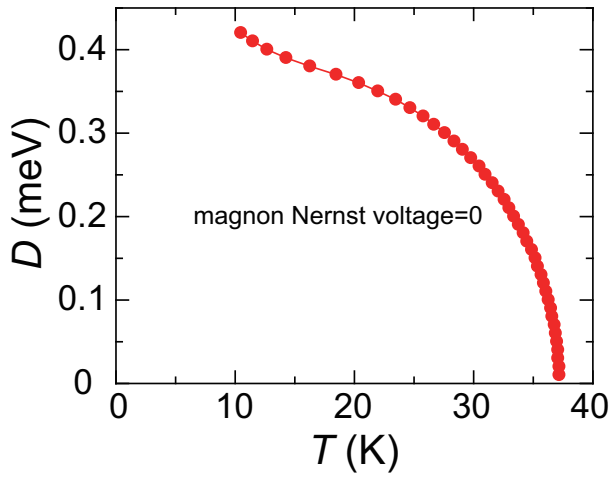

FIG. 7: The sign-change temperature of the magnon Nernst coefficient which is calculated as a function of the Dzyaloshinskii-Moriya (DM) parameter.

since both temperature gradient and spin current are odd under the inversion of $(x,\ y,\ z) \rightarrow (-x,\ -y,\ -z)$. Furthermore, different Néel states in bulk $MnPS_3$ are connected by the inversion operation, and hence α^s_{xy} is considered to be the same for the different domains. For monolayer $MnPS_3$, similar arguments are also valid using C_2 rotation symmetry.

We can explicitly show this argument by microscopic calculations. Since the strength of

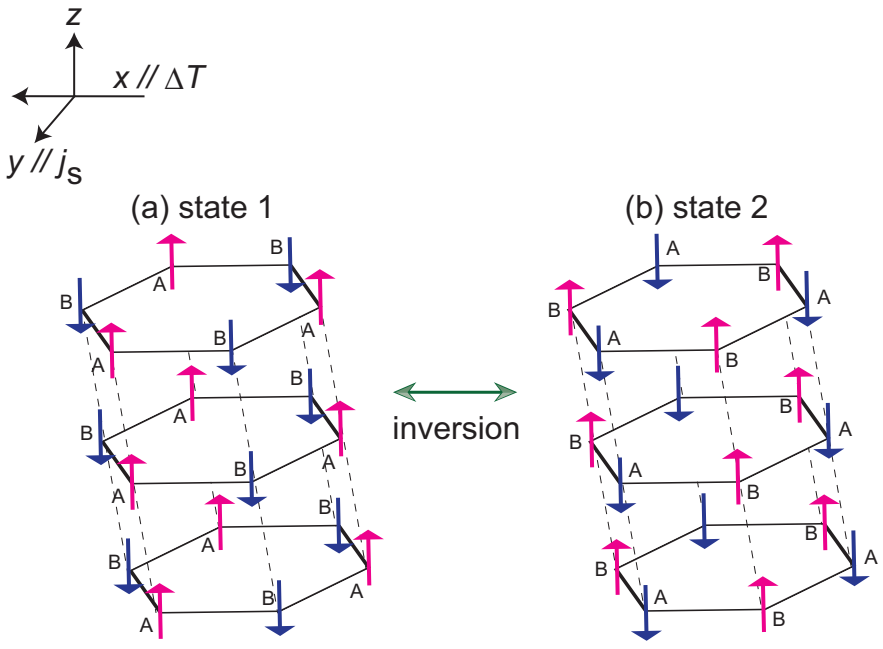

FIG. 8: Two Néel states in $MnPS_3$: (a) state 1 and (b) state 2.

the interlayer exchange coupling is two orders of magnitude smaller than that of intralayer exchange coupling [13], we here discuss the magnon Nernst effect for monolayer $MnPS_3$. As shown in [10, 11], α^s_{xy} is calculated using the Berry curvature and the energy dispersion of magnons. Using the same model as studied in [10], we consider two Néel states: state 1 ($\boldsymbol{S}_{iA} = -\boldsymbol{S}_{iB} = S\hat{\boldsymbol{z}}$) and state 2 ($\boldsymbol{S}_{iA} = -\boldsymbol{S}_{iB} = -S\hat{\boldsymbol{z}}$), where $\boldsymbol{S}_{iA(B)}$ is the spin operator on the A (B) sublattices (Fig. 8). To derive the magnon modes, we first apply the Holstein-Primakoff transformation for each state:

$$\begin{cases} S^+_{iA} \approx \sqrt{2S}a_i, \quad S^z_{iA} = S - a^\dagger_i a_i, \quad S^+_{iB} \approx \sqrt{2S}b^\dagger_i, \quad S^z_{iB} = b^\dagger_i b_i - S, & \text{(for state 1)} \\ S^+_{iA} \approx \sqrt{2S}a^\dagger_i, \quad S^z_{iA} = a^\dagger_i a_i - S, \quad S^+_{iB} \approx \sqrt{2S}b_i, \quad S^z_{iB} = S - b^\dagger_i b_i. & \text{(for state 2)} \end{cases}$$

Here we emphasize that $a_i(b_i)$ carries the opposite spin angular momentum along $\hat{z}$ between states 1 and 2. The spin Hamiltonian can be expressed with these operators, and the only difference in the Hamiltonian between states 1 and 2 is the sign of the second nearest-neighbor DM interaction (D) given by

$$\begin{cases} +SD\sum_{\boldsymbol{k}} g(\boldsymbol{k}) \left(a^\dagger_{\boldsymbol{k}} a_{\boldsymbol{k}} - b^\dagger_{\boldsymbol{k}} b_{\boldsymbol{k}} \right), & \text{(for state 1)} \\ -SD\sum_{\boldsymbol{k}} g(\boldsymbol{k}) \left(a^\dagger_{\boldsymbol{k}} a_{\boldsymbol{k}} - b^\dagger_{\boldsymbol{k}} b_{\boldsymbol{k}} \right), & \text{(for state 2)} \end{cases}$$

where $a_{\boldsymbol{k}} = \frac{1}{\sqrt{N}}\sum_i a_{\boldsymbol{i}} e^{-i\boldsymbol{k}\cdot\boldsymbol{R}_i}$, $b_{\boldsymbol{k}} = \frac{1}{\sqrt{N}}\sum_i b_i e^{i\boldsymbol{k}\cdot\boldsymbol{R}_i}$, and $g(\boldsymbol{k}) = -g(-\boldsymbol{k})$ depends on the vectors that connect second nearest neighbors [10].

After a Bogoliubov transformation, we obtain two magnon modes with $S^z = \pm 1$, where $S^z = \sum_i (S^z_{iA} + S^z_{iB})$ is a good quantum number in the current system. Notably, the energy dispersions for the two modes are found to be the same between states 1 and 2 as $\hbar\omega^{(1)}_{\uparrow/\downarrow}(\boldsymbol{k}) = \hbar\omega^{(2)}_{\uparrow/\downarrow}(\boldsymbol{k})$, where $\hbar\omega^{(i)}_{\uparrow}(\boldsymbol{k})$ ($\hbar\omega^{(i)}_{\downarrow}(\boldsymbol{k})$) is the energy dispersion of the magnon with spin $S^z = +1(-1)$ for state i. The same energy dispersions for states 1 and 2 result from the fact that both the signs of the spin angular momentum along $\hat{z}$ and D are opposite between states 1 and 2. Since the Berry curvature does not depend on either D or S^z carried by each mode, the Berry curvature is also the same for states 1 and 2. Therefore, the magnon Nernst coefficient is the same for different Néel domains.

Appendix E: The relation between Pt resistivity and potential magnon Nernst signal

In Fig. 9, the relation between two-wire Pt resistivity $\rho_{\rm Pt}^{\rm 2w}$ and low-temperature thermoelectric signal $S_{\rm Pt}$ is investigated for various Pt|$MnPS_3$ samples. As shown in Fig. 9(a), for Pt|$MnPS_3$ samples whose $\rho_{\rm Pt}^{\rm 2w}$ is larger than 5×10^{-5} Ωcm, $S_{\rm Pt}$ has a positive sign in all the T range, and monotonically decreases toward zero when $T \to 0$. In contrast, for relatively low-$\rho_{\rm Pt}^{\rm 2w}$ samples, where $\rho_{\rm Pt}^{\rm 2w}$ is almost smaller than 5×10^{-5} Ωcm (but larger than $\rho_{\rm Pt}^{\rm 2w}$ of Pt2 of Sample1), $S_{\rm Pt}$ shows a sign change from positive to negative at low temperatures, as shown in Fig. 9(b). This sign change observed for relatively low-$\rho_{\rm Pt}^{\rm 2w}$ samples at low temperatures may be attributed to the magnon Nernst signal, as observed in Pt2 of Sample1 (Fig. 3).

It is noted that, for a reference Pt sample grown on a diamagnetic $SrTiO_3$ substrate whose $\rho_{\rm Pt}^{2w}$ magnitude is comparable to that of Pt2 of Sample1 [see Fig. 9(a)], the thermoelectric coefficient is positive in the entire T regime, and does not show a sign change, as shown in Fig. 9(c). The overall temperature dependence is similar to that observed in high-$\rho_{\rm Pt}^{2w}$ samples shown in Fig. 9(a). Also, we confirmed that the sign change is not observed in a Pt|SiO_2 sample.

Appendix F: Data reproducibility in the measurements of magnetoelectric-cooling dependence

We confirmed that, after all the measurements of the magnetoelectric (ME) cooling dependence (Fig. 4), the $S_{\rm Pt}$ values measured without the ME cooling for Sample2 return to the original $S_{\rm Pt}$ values, as shown by green triangles in Fig. 10. By the ME cooling, the $S_{\rm Pt}$ values for Sample2 decrease in the T range between 30 K and 50 K, as discussed in Fig. 4. Then, after all the measurements of the ME-cooling dependence, we again measured the T dependence of $S_{\rm Pt}$ without any ME cooling. As shown in Fig. 10, the obtained $S_{\rm Pt}$ values (green color) return to the original values (black color), which supports the reliability of the measurements of the ME-cooling dependence.

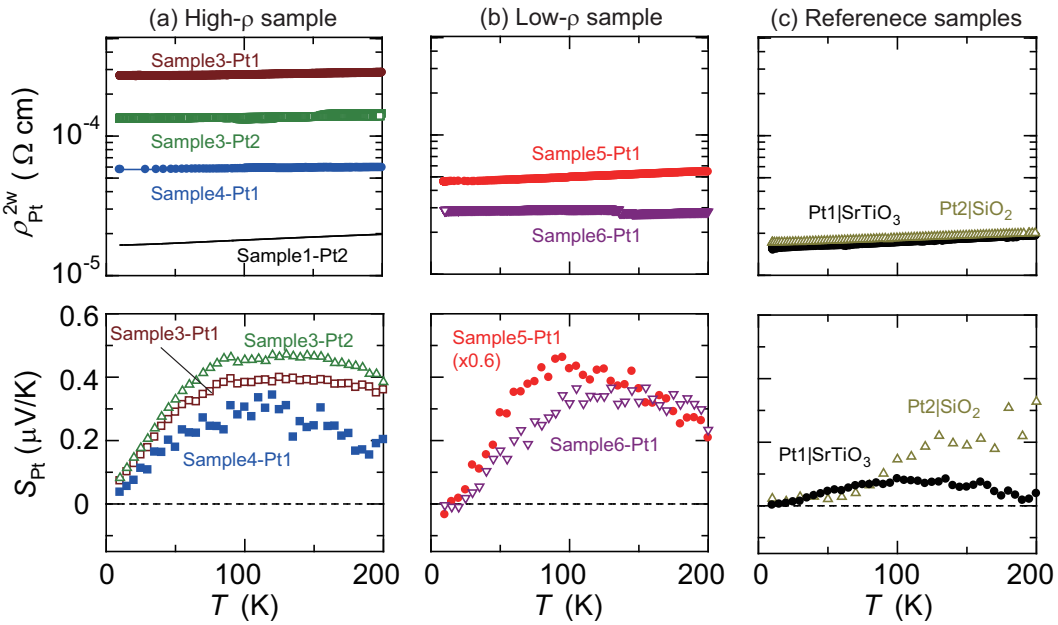

FIG. 9: Temperature (T) dependence of the two-wire resistivity ($\rho_{\rm Pt}^{\rm 2w}$) and the thermoelectric coefficient ($S_{\rm Pt}$) for (a) high-$\rho_{\rm Pt}^{\rm 2w}$ Pt|$MnPS_3$ samples ($\rho_{\rm Pt}^{\rm 2w} \gtrsim 5\times10^{-5}$ Ωcm), (b) low-$\rho_{\rm Pt}^{\rm 2w}$ Pt|$MnPS_3$ samples ($\rho_{\rm Pt}^{\rm 2w} \lesssim 5\times10^{-5}$ Ωcm), and (c) refernece Pt samples, Pt1|$SrTiO_3$ and Pt2|SiO_2.

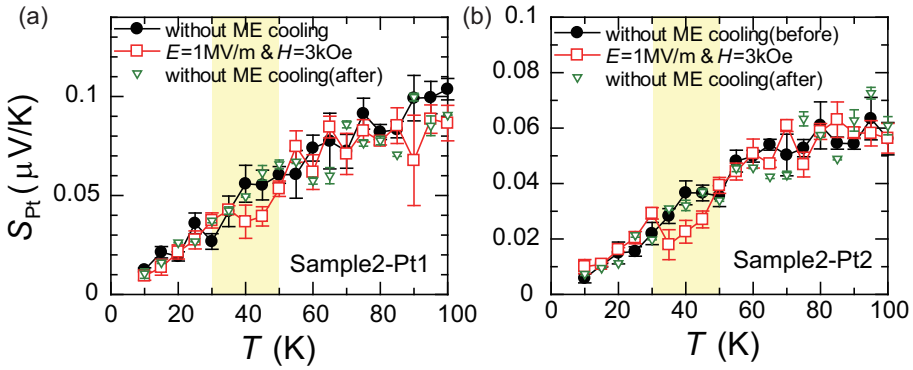

FIG. 10: Temperature (T) dependence of $S_{\rm Pt}$ for (a) Pt1 of Sample2 and (b) Pt2 of Sample2, measured without the ME cooling (black dots: measurement results obtained before the ME cooling experiments; green triangles: measurement results obtained after the ME cooling experiments) and with the ME cooling (red squares).

[1] D. Xiao, M.-C. Chang, and Q. Niu, Rev. Mod. Phys. **82**, 1959 (2010).

[2] N. Nagaosa, J. Sinova, S. Onoda, A. H. MacDonald, and N. P. Ong, Rev. Mod. Phys. **82**, 1539 (2010).

[3] J. Sinova, S. O. Valenzuela, J. Wunderlich, C. H. Back, and T. Jungwirth, Rev. Mod. Phys. **87**, 1213 (2015).

[4] H. Katsura, N. Nagaosa, and P. A. Lee, Phys. Rev. Lett. **104**, 066403 (2010).

[5] R. Matsumoto and S. Murakami, Phys. Rev. Lett. **106**, 197202 (2011).

[6] Y. Onose, T. Ideue, H. Katsura, Y. Shiomi, N. Nagaosa, Y. Tokura, Science **329**, 297 (2010).

[7] T. Ideue, Y. Onose, H. Katsura, Y. Shiomi, S. Ishiwata, N. Nagaosa, and Y. Tokura, Phys. Rev. B **85**, 134411 (2012).

[8] M. Hirschberger, R. Chisnell, Y. S. Lee, and N. P. Ong, Phys. Rev. Lett. **115**, 106603 (2015).

[9] T. Ideue, T. Kurumaji, S. Ishiwata, and Y. Tokura, Nature. Mater. *in press. (advance online publication)* (2017).

[10] R. Cheng, S. Okamoto, and D. Xiao, Phys. Rev. Lett. **117**, 217202 (2016).

[11] V. A. Zyuzin and A. A. Kovalev, Phys. Rev. Lett. **117**, 217203 (2016).

[12] O. Gomonay, T. Jungwirth, and J. Sinova, Phys. Status Solidi RRL **11**, 1700022 (2017).

[13] A. R. Wildes, B. Roessli, B. Lebech, and K. W. Godfrey, J. Phys.: Condens. Matter **10**, 6417 (1998).

[14] K. Kurosawa, S. Saito, and Y. Yamaguchi, J. Phys. Soc. Jpn. **52**, 3919 (1983).

[15] R. Brec, Solid State Ionics **22**, 3 (1986).

[16] E. Saitoh, M. Ueda, H. Miyajima, and G. Tatara, Appl. Phys. Lett. **88**, 182509 (2006).

[17] K. Okuda, K. Kurosawa, S. Saito, M. Honda, Z. Yu, and M. Date, J. Phys. Soc. Jpn. **55**, 4456 (1986).

[18] Y. Shiomi, T. Ohtani, S. Iguchi, T. Sasaki, Z. Qiu, H. Nakayama, K. Uchida, and E. Saitoh, Appl. Phys. Lett. **104**, 242406 (2014).

[19] J. P. Moore and R. S. Graves, J. Appl. Phys. **44**, 1174 (1973).

[20] R. D. Barnard, *Thermoelectricity in Metals and Alloys*, Taylor & Francis Ltd. (1972).

[21] C. L. Foiles, J. Phys. F: Met. Phys. **8**, 213 (1978).

[22] A. I. Schindler, and B. R. Coles, J. Appl. Phys. **39**, 956 (1968).

[23] P. Zolotavin, C. I. Evans, and D. Natelson, Nanoscale **9**, 9160-9166 (2017).

[24] P. Zolotavin, C. Evans, and D. Natelson, J. Phys. Chem. Lett. **8**, 1739-1744 (2017).

[25] E. Ressouche, M. Loire, V. Simonet, R. Ballou, A. Stunault, and A. Wildes, Phys. Rev. B **82**, 100408 (2010).

[26] S. Seki, Y. Yamasaki, Y. Shiomi, S.Iguchi, Y. Onose, and Y. Tokura, Phys. Rev. B **75**,

100403(R) (2007).